PART V

Appendix

A

Radar and Its Applications

A.1 Radar basics

Radars are arguably the most important mesoscale meteorological observing systems. It is virtually impossible to study mesoscale phenomena observationally without analyzing radar data at some point. Recall from Chapter 1 that the first use of the term *mesoscale* was in a radar paper highlighting observations of subsynoptic-scale meteorological phenomena.

A weather radar works by transmitting electromagnetic waves (microwaves) that interact with hydrometeors as the waves propagate through the atmosphere. The radar's transmitter produces power at a known frequency (3-10 GHz for most weather radars), and the transmitted waves are focused into a beam (typically $1-2^{\circ}$ wide) by an antenna. When the radar beam intercepts a particle, called a target, some of the energy is absorbed and some is scattered. The amount that is scattered depends on the shape and dielectrical properties of the scatterer (i.e., its refractive index) and on the ratio of the wavelength of the transmitted energy to the size of the scatterer. When the diameter of the target (e.g., a raindrop) is very small compared with the wavelength, the scattered energy is proportional to the sixth power of the diameter of the target. This is sometimes referred to as the Rayleigh scattering regime. In contrast, when the target diameter is large relative to the wavelength, sometimes called the Mie scattering regime, the relationship between the scattered energy and target diameter is considerably more complicated and cannot be expressed as a simple function of target size.

Only a small fraction of the energy transmitted by the radar is backscattered by targets to the radar's antenna; most of the scattering is in directions that do not intersect the antenna. The radar's receiver detects, amplifies, and converts the reflected signal into a low-frequency signal. The receiver must be very sensitive—the transmitted power of a radar is typically between 250 and 1000 kW, yet the backscattered power that reaches the receiver may only be $\sim 10^{-16}$ kW, that is, 18 orders of magnitude less than was transmitted! Furthermore, the receiver must be able to detect a wide range of backscattered power. The backscattered power can vary by nine orders of magnitude, depending on whether the radar is observing large hail or dust.

The most popular quantity related to returned power probably is the *logarithmic reflectivity factor*,

$$Z = 10 \log_{10} \left(\frac{z}{1 \text{ mm}^6/\text{m}^3} \right),$$
 (A.1)

where z is the *reflectivity factor*, which has units of mm⁶ m⁻³ (z is the summation over a volume of the sixth power of target diameters), and Z is measured in units of dBZ (i.e., decibels relative to a reflectivity factor of 1 mm⁶ m⁻³).

The reflectivity factor is related to the *received backscattered power*, P_r , via

$$z = C P_r r^2, \tag{A.2}$$

where C, known as the *radar constant*, depends on the attributes of the radar (e.g., wavelength, antenna characteristics, losses of power in the radar, etc.) and r is the distance to the target. Therefore, the reflectivity factor

 $^{^{1}}$ It is hard for most of us to grasp just how large a span of 18 orders of magnitude is. It represents the difference between the diameter of a dime ($\sim 10^{-2}$ m) and the distance to the nearest star outside of our solar system ($\sim 10^{16}$ m), which itself is hard for most of us to grasp.

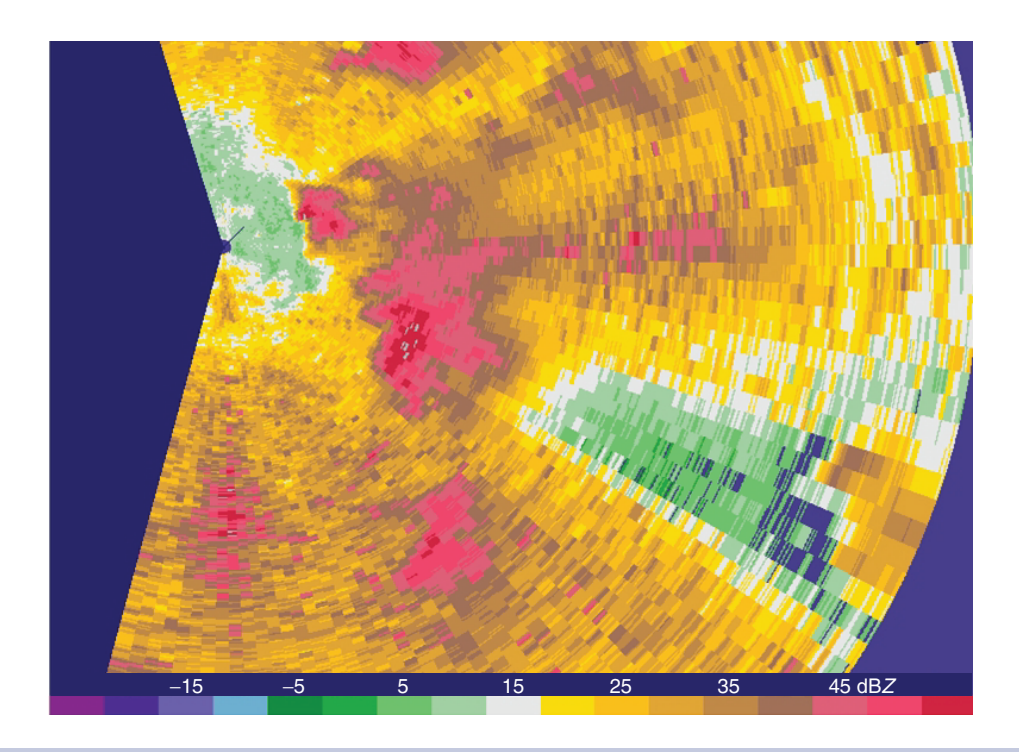


Figure A.1 When relatively short wavelengths are used, both scattering and absorption are significant, and attenuation can be severe. In this example, a 5-cm radar mounted in the tail section of an aircraft is scanning a broken line of severe thunderstorm from the west. Significant loss of power is occurring within the heavy precipitation core (which likely contains large hail) located southeast of the radar; thus, the reflectivity at ranges beyond this heavy precipitation core has been underestimated.

can be viewed as a range-corrected measure of received power (there is an r^{-2} reduction in the power that is backscattered to the radar).

In addition to being sensitive to the size of the targets, the logarithmic reflectivity factor (hereafter referred to as reflectivity²) depends on the number of targets encountered by the electromagnetic pulse (high reflectivity implies heavier precipitation, if all else is equal). As the transmitted or backscattered radiation passes through the air, cloud, rain, etc., some of the energy is absorbed or scattered in other directions. This loss of power along the path of the radar beam is called *attenuation*, and it is most pronounced for radar using wavelengths less than 10 cm (Figure A.1).

To detect returns at various radar ranges, the returned signals are 'gated' (i.e., sampled periodically), usually approximately every $0.1{-}1~\mu s$, to obtain information

roughly every few tens or hundreds of meters in range. This sampling can go on until it is time to transmit the next pulse. The frequency at which pulses are transmitted by the radar is called the *pulse repetition frequency*, or PRF. Most radars have a PRF on the order of 1000 Hz. For a PRF of 1000 Hz, it is possible to acquire 1000 1-µs samples between pulses. A sample point in time is called a *range gate*.

The factors that govern the choice of a wavelength to be used in a particular radar include the radar's desired sensitivity (i.e., the ability to detect weak targets at long range), the radar's ability to resolve small features, the types of targets to be studied, and the effect of the intervening atmosphere on the transmitted energy (i.e., attenuation). Other factors must also be considered, such as the cost, size, and weight of the radar. Most weather radars have wavelengths that range from 0.8–10.0 cm. Short-wavelength radars are generally smaller and less expensive to build. Furthermore, at short wavelengths (e.g., 3–5 cm or smaller), a narrow beam (1° or less) can be produced by a smaller antenna. As wavelength increases, antenna size also increases if the beamwidth is held fixed. However, the shorter the

² Even though reflectivity and logarithmic reflectivity factor are two different things as defined above, the use of the term *reflectivity* in place of *logarithmic reflectivity factor* has become so commonplace that most assume *logarithmic reflectivity factor* is implied when the term *reflectivity* is used, unless it is otherwise obvious from the context.

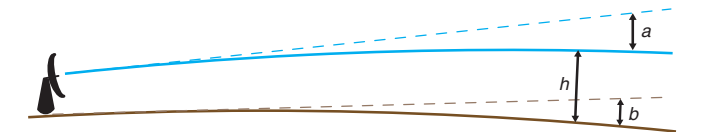


Figure A.2 Effect of Earth's curvature and refraction on the height of distant targets above the ground. The solid blue line is the path of the transmitted and reflected beam, and the solid brown line is the Earth's surface (the curvature is somewhat exaggerated for illustrative purposes). The dashed blue line is the path that the beam would take in the absence of refraction. The dashed brown line represents the line tangent to the Earth's surface at the location of the radar. The Earth's radius and oblateness determine a, and the variation of static stability along the beam determines b (usually a standard atmosphere is assumed). The height of targets above the ground (h) is known if a and b are known.

wavelength, the greater the attenuation. Short-wavelength radars are more effective in detecting small particles such as cloud droplets and drizzle droplets; however, as mentioned above, attenuation becomes more severe than when longer wavelengths are used, owing to scattering *and* absorption. Thus, it may be difficult to accurately measure the intensity of backscattered energy from distant targets. The main advantage of using longer wavelengths is that absorption by the intervening particles is drastically reduced. For example, the Weather Surveillance Radar-1988 Doppler (WSR-88D) used by the United States National Weather Service operates with a 10-cm wavelength, which is relatively immune to substantial attenuation.

The radar needs three pieces of information to determine the location of a target: azimuth angle (the angle of the radar beam with respect to north), elevation angle (the angle of the beam with respect to the horizon), and the distance from the radar to the target. The distance to the target is determined by measuring the time it takes for the pulse to complete a round trip from the radar to the target and back, that is,

$$r = \frac{ct}{2},\tag{A.3}$$

where c is the speed of light (3 × 10⁸ m s⁻¹), which is the speed at which the radar pulses travel, and t is the time that elapses between the transmission of the pulse and the reception of backscattered energy from the target.

One must account for the curvature of the Earth when determining the altitude of a target. Distant targets that are close to the ground cannot be seen by a radar because they will be below the horizon. The height of a distant target that is above the horizon will be underestimated if the curvature of the Earth is not considered.

Refraction also affects the path that transmitted electromagnetic energy takes as it propagates through the atmosphere. The degree to which the radar beam is bent depends on how the refractive index, which is a strong

function of the air density, varies with height.³ In most situations the refractive index decreases with height, which causes the radar beam to be deflected downward. Usually a standard atmosphere temperature profile is assumed when computing beam height; thus, departures from this stratification lead to errors in the vertical placement of targets. In extreme cases, such as when a strong temperature inversion is present, the radar beam can be bent downward so much that it intersects the ground. This effect is called *anomalous propagation*, and it results in the appearance of ground targets on the radar display that would not normally appear.

A.2 Doppler radar principles

A.2.1 Radial velocity and spectrum width

In Doppler radars, the phase of the backscattered signal is detected, and, when it is compared with the returned phase of the previous pulse, a *radial velocity*—the component of the target's velocity parallel to the radar beam—can be computed. A phase shift is observed between subsequent pulses if a target is moving. The phase shift, $\Delta \phi$, is a result of differences in the distance a wave must travel from one pulse to the next. It can be shown that

$$\Delta \phi = \frac{4\pi \,\Delta r}{\lambda},\tag{A.4}$$

where $\Delta \phi$ is measured in radians, Δr is the distance the target travels between pulses (positive (negative) if the target is moving away from (toward) the radar), and λ is the wavelength of the radar. The radial velocity, v_R , is

³ The refractive index, n, is often expressed in terms of *refractivity*, N, where $N=(n-1)\times 10^6$. For example, n=1.0003 corresponds to N=300; N varies from ~ 400 near the surface to ~ 200 in the middle troposphere in typical warm-season conditions.

Figure A.3 Example of spectrum width imagery (right; reflectivity is on the left) of a supercell thunderstorm in central Pennsylvania. Here the spectrum width, or the standard deviation of the radial velocity measurements within a sample volume (scale has units of m s⁻¹), can be used to make inferences about the turbulence within the storm and its near environment. The inflow region of the storm (to the east-northeast) is characterized by low spectrum width values, implying fairly laminar flow, which is what might be expected in a region of horizontal accelerations, which increase helicity and suppress turbulence. The hook echo region (where the rear-flank downdraft is located), on the other hand, is characterized by large spectrum width values, implying larger turbulence there. This also might be anticipated, owing to the fact that downdrafts are driven, at least in part, by entrainment, which tends to promote turbulence.

related to the phase shift via

$$v_{\rm R} = \frac{\Delta r}{\Delta t} = \frac{\lambda}{4\pi} \frac{\Delta \phi}{\Delta t},\tag{A.5}$$

where Δt is the time between pulses, known as the *pulse* repetition time, or PRT, where PRT = PRF⁻¹. Motion of a target toward (away from) a radar has a negative (positive) radial velocity.

When one views a radial velocity display, it is the mean velocities in the radar sample volumes that are being displayed. The variance of the radial velocity measurements in a sample volume is related to the *spectrum width*, which is a function of the spread of the terminal fall speeds of scatterers, turbulence within the sample volume, and shear of the wind along or across the beam. Spectrum width is also often used as a measure of data quality; spectrum width is falsely large when the returned signals are weak. Spectrum width imagery of a supercell thunderstorm is shown in Figure A.3.

A.2.2 Range and velocity folding

The pulses of transmitted energy are separated in space by a distance R, which is related to the PRF by R = c/PRF.

When radiation is backscattered off a far-away target and received at the radar *after* radiation from the next pulse has been sent, *range-folding* occurs, and it is not known whether the radar echo represents a target nearby or far away (Figures A.4 and A.5). The maximum range

10.10027280470682104.app, I. Downloaded from https://onlinelbrlary.wiley.com/doi/10.10027980470682104.app1 by University Of Newada Reno. Wiley Online Library on [1901/2024]. See the Terms and Conditions (https://onlinelbrlury.wiley.com/terms-and-conditions) on Wiley Online Library or rules of use. OA articles are governed by the applicable Certain Common License

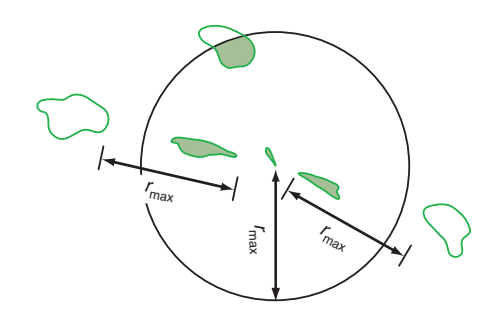


Figure A.4 Illustration of range-folding. Radar echoes beyond the maximum unambiguous range $(r_{\rm max})$ (unshaded echoes) are *folded* back into the area within the maximum unambiguous range. Echoes actually located within the maximum unambiguous range, as well as folded echoes, are both shaded.

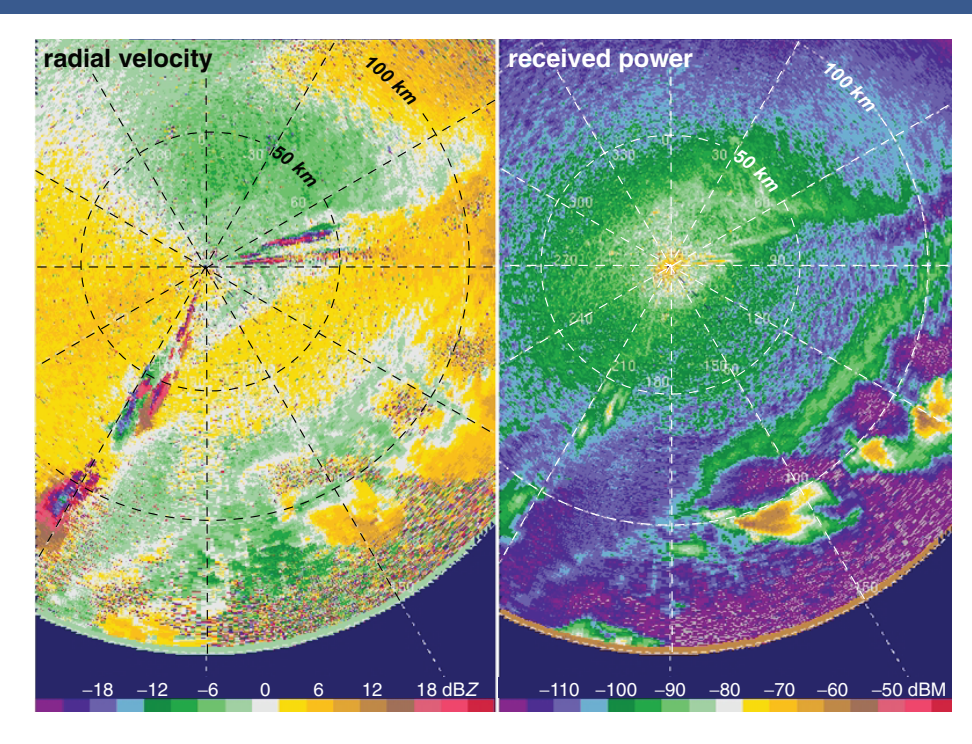


Figure A.5 Example of range-folding in imagery obtained by the National Center for Atmospheric Research (NCAR) S-POL radar on 12 June 2002 during the International $\rm H_2O$ Project (IHOP). Radial velocity (m s⁻¹) is displayed on the left and received power (dBm; dBm = $\rm 10 \log_{10}(P_r/1~mW)$) is displayed on the right. A trio of thunderstorms is unambiguously detected to the southeast of the radar. These thunderstorms developed along a northeast–southwest-oriented mesoscale convergence line. Additional thunderstorms developed along the line farther to the northeast and southwest (the extreme northern edge of one is barely visible at approximately 190° near the maximum range of $150~\rm km$), but beyond the radar's maximum unambiguous range. These echoes are displayed as second-trip echoes near 200° and 210° at approximately $70-80~\rm km$ range, near 215° at a range of approximately $110~\rm km$, and at $75-85^\circ$ at ranges of approximately $20-50~\rm km$. Note the anomalous radial velocities in the region of range-folded echoes, in addition to the unusually elongated shapes of the range-folded echoes.

at which the location of echoes may be determined unambiguously is

$$r_{\text{max}} = \frac{c}{2 \text{ PRF}}.$$
 (A.6)

Echoes at a range of $r_{\rm max} + nc/2{\rm PRF}$ (where n is a positive integer) are received by the receiver at the same time as echoes at $r_{\rm max}$. Distant, second-trip echoes (echoes located between $r = r_{\rm max}$ and $r = 2r_{\rm max}$) can be distinguished by their elongated appearance since their angular width is preserved when displayed at their apparent, incorrect range. A Range-folding can be identified (and removed)

algorithmically) by interlacing signals having different PRFs. When the PRF changes, range-folded echoes appear to move, whereas *first-trip* echoes (echoes located at range $r < r_{\text{max}}$) remain stationary.

The sampling rate of the returned signal (i.e., the PRF) is important in detecting the phase shift of the signal. If the sampling rate (PRF) is too slow, a large phase shift can be *aliased* (i.e., it will appear to have a much smaller phase shift than it actually has, resulting in an incorrect radial velocity value). Thus, a maximum unambiguous velocity also exists. It is related to the PRF and wavelength by

$$v_{\rm Rmax} = \pm \frac{({\rm PRF}) \,\lambda}{4}.$$
 (A.7)

All velocities exceeding these bounds are aliased or *folded* onto other portions of the velocity spectrum (Figure A.6).

⁴ Third-trip echoes (echoes located between $r=2r_{\rm max}$ and $r=3r_{\rm max}$) are rare because the radar beam usually overshoots echoes at such long ranges.

Figure A.6 Example of velocity aliasing during the landfall of Hurricane Isabel (2003) along the coast of North Carolina. Reflectivity is displayed on the left, and radial velocity is displayed on the right. Range rings are at 15 km intervals and azimuth spokes are at 30° intervals. The eye of the hurricane is approximately 75 km east of the radar, and the strong northerly winds at the radar have been aliased in the regions \sim 60 km north of the radar (where yellow outbounds are erroneously displayed) and \sim 60 km south-southeast of the radar (where green inbounds are erroneously displayed).

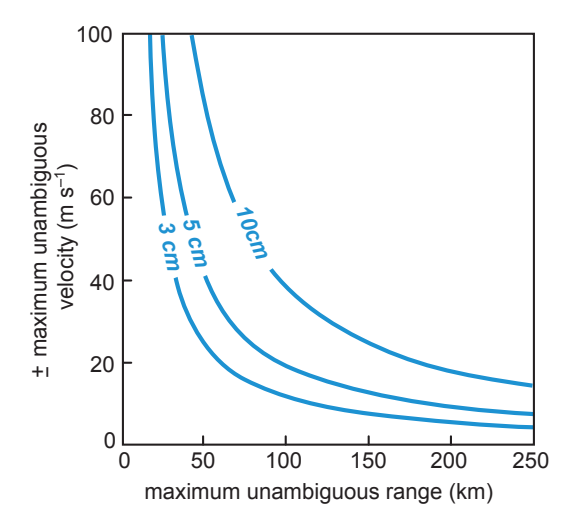


Figure A.7 Relationship between maximum unambiguous range and maximum unambiguous Doppler velocity for radars transmitting at wavelengths of 3, 5, and 10 cm.

The interval given by (A.7) is also called the *Nyquist* interval, with $v_{\rm Rmax}$ also sometimes called the *Nyquist* velocity.

Increasing the PRF to extend v_{Rmax} decreases r_{max} . This limitation is popularly referred to as the *Doppler dilemma*.

We can combine (A.6) and (A.7) to illustrate this:

$$v_{\rm Rmax} r_{\rm max} = \pm \frac{\lambda c}{8}.$$
 (A.8)

10.10027280470682104.app, I. Downloaded from https://onlinelbrlary.wiley.com/doi/10.10027980470682104.app1 by University Of Newada Reno. Wiley Online Library on [1901/2024]. See the Terms and Conditions (https://onlinelbrlury.wiley.com/terms-and-conditions) on Wiley Online Library or rules of use. OA articles are governed by the applicable Certain Common License

From (A.8) and Figure A.7 we see that the PRF and wavelength must be chosen carefully. In addition, the wavelength must not be too long, or else precipitation and clouds will not be detected owing to weak backscattering. On the other hand, if the wavelength is too small, attenuation will limit range.

A.3 Applications

A.3.1 Clear-air returns

When a radar transmits energy, part of it may be intercepted by targets on the ground, such as buildings, trees, power lines, or other objects. This *ground clutter* interferes with the detection of meteorological targets because ground targets are large and typically produce high reflectivity. Ground clutter can result even if the main radar beam is above ground targets, because part of the energy radiated from the antenna is emitted off the beam axis in what are known as *sidelobes*. Backscattered energy from the sidelobes is interpreted by the radar processor to come from the main lobe; thus, ground targets hit by one of the sidelobes

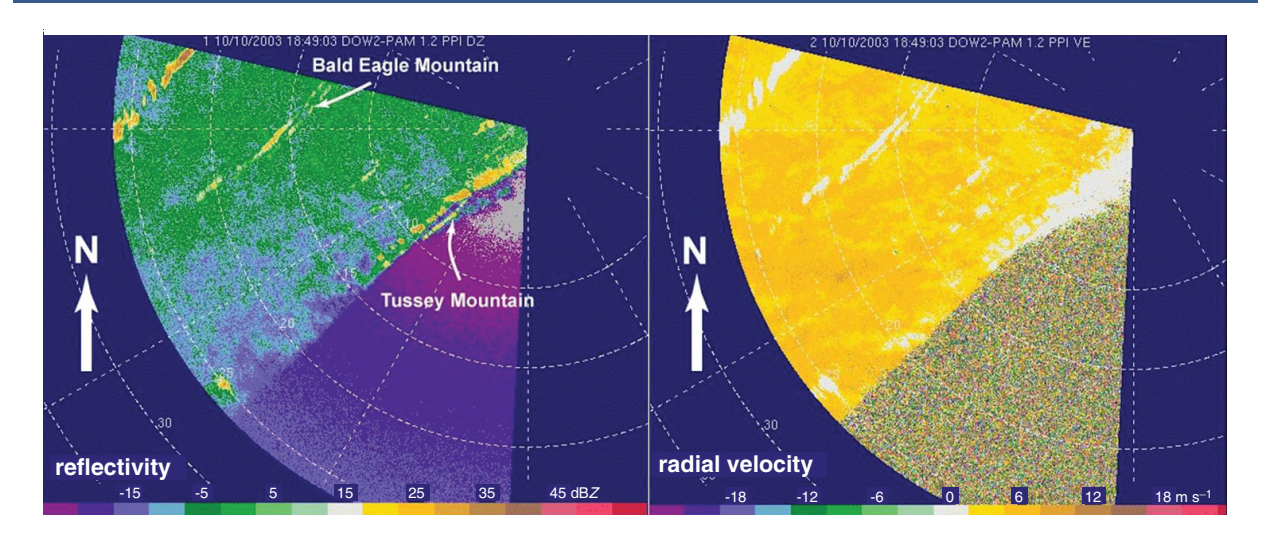


Figure A.8 Example of ground clutter in radar imagery obtained by the Doppler On Wheels (DOW) radar southwest of State College, PA. Reflectivity is displayed on the left and radial velocity is displayed on the right. Range rings are at 5 km intervals and azimuth spokes are at 30° intervals. At locations where the radar beam intersects mountains, reflectivities are large and radial velocities are approximately zero. The echoes from the valley between the two mountain ridges are largely from insects.

appear to a radar user in the same relative position in the main lobe.

Ground clutter is usually worst within about 20 km of the radar, where the beam is still close to the earth's surface. Farther from the radar, the beam is higher owing to both its elevation angle and the curvature of the earth (Figure A.2). Ground clutter is easily identified with a Doppler radar because the radial velocity measured by the Doppler radar is approximately zero (most ground targets are stationary; Figure A.8). The radial velocity may not be exactly zero because moving targets within the beam, such as birds, airborne insects, and raindrops, also contribute to the total power returned to the radar.

Airborne insects, which are commonly detected by weather radars during the warm season, are among the most important clear-air returns. They are excellent tracers of air motion because, on average, airborne insects move with the wind (Figures A.8). The echoes from insects can reveal convergence zones (e.g., drylines, outflow boundaries, fronts) as reflectivity fine-lines, where deep convection may be most likely to be initiated or where existing storms could interact with a zone of enhanced wind shear (Figure A.9). Clear-air returns can also be obtained from regions containing fluctuations in the refractive index of the air due to turbulence. This is called *Bragg scattering*.

A.3.2 Interpreting Doppler velocity patterns

To understand Doppler radial velocity patterns, one first has to consider the geometry of a radar scan. Normally the radar beam is pointed at an elevation angle greater than zero so that the beam height increases with range. Because of this geometry, radar returns originating from targets near the radar detect the low-level wind field, whereas returns from distant targets detect the wind field at higher levels. To determine the horizontal wind at a particular elevation above the radar, one can examine the radial velocities on a constant-range ring encircling the radar. The elevation represented by a particular constant-range ring depends upon the elevation angle of the radar beam.

In the examples that follow, idealized Doppler radial velocity patterns were constructed assuming simple vertical wind profiles. These simplified radial velocity patterns can serve as a starting point from which inferences can be made from observations of more complicated patterns. Doppler velocity patterns (right) correspond to vertical wind profiles (left), where the wind barbs indicate wind speed and direction from the ground up to 8 km. Negative Doppler velocities (blue shades) are toward the radar and positive (red shades) are away. The radar location is at the center of the display.

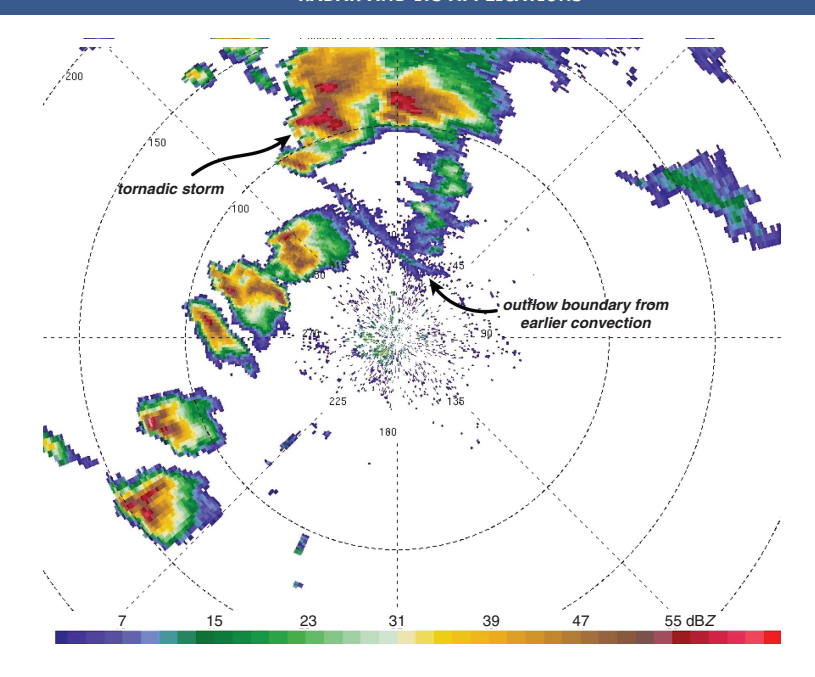


Figure A.9 Lowest-elevation-angle reflectivity from the Lubbock, TX, radar at 0102 UTC 3 June 1995. A reflectivity fine-line is associated with an outflow boundary produced by convection occurring a few hours earlier. Many of the subsequent storms that crossed this outflow boundary became tornadic. Vertical wind shear and low-level humidity were enhanced along and on the immediate cool side of the outflow boundary. This is the same case as shown in Figure 10.15.

In Figure A.10a, wind direction is constant with height, but wind speed increases from 10 kt at the ground to 40 kt at 8 km. Note that the maximum inbound velocity is to the west and maximum outbound velocity is to the east. The radar measures zero radial velocity to the north and south because the winds are perpendicular to the radar beam when the beam is directed toward the north or south. In Figure A.10b, the winds increase from 10 to 40 kt between the surface and 4 km, and then decrease again to 10 kt at 8 km. The wind direction is again constant with height. The radar beam intersects the 4 km level at a range of approximately 50 km, where the maximum inbound and outbound velocities are observed.

Figure A.11a displays the Doppler velocity field for the case of winds that back from northerly at the ground to westerly at 8 km; wind speed is a constant with height. Note the characteristic backward 'S' shape of the zero-velocity line. In Figure A.11b, the interpretation is exactly the opposite of that in Figure A.11a. The winds veer with height and the zero line takes the shape of a forward 'S.' In Figure A.12, winds veer with height to 4 km and then back with height to 8 km, resulting in a forward 'S' pattern within 50 km range and a backward 'S' beyond 50 km range.

When the wind field is horizontally uniform, the radial velocity sampled along a constant range ring varies sinusoidally with azimuth. However, the wind field commonly is not horizontally uniform; in such instances, the radial velocity sampled along a constant range ring does not vary sinusoidally with azimuth. There may even be rather pronounced asymmetries in the radial velocity field, especially if an abrupt wind shift (e.g., along a front) is sampled by the radar. Figure A.13 presents idealized Doppler velocity displays for the cases of a difluent wind field, a confluent wind field, and a front associated with a 90° wind shift.

Nonuniformity in the wind field may exist on much smaller scales as well; for example, in an isolated thunderstorm there may be locally strong low-level convergence and/or divergence (e.g., beneath the updraft or within a microburst, respectively), or perhaps a mesocyclone. Figure A.14 displays what a uniform westerly wind field would look like in a subdomain of the regions displayed in Figures A.10–A.13. Figure A.15 displays idealized Doppler velocity patterns for the case of a mesocyclone having cyclonic vorticity (Figure A.15a), a purely convergent wind field (Figure A.15b), and a wind field consisting of roughly equal amounts of cyclonic vorticity and

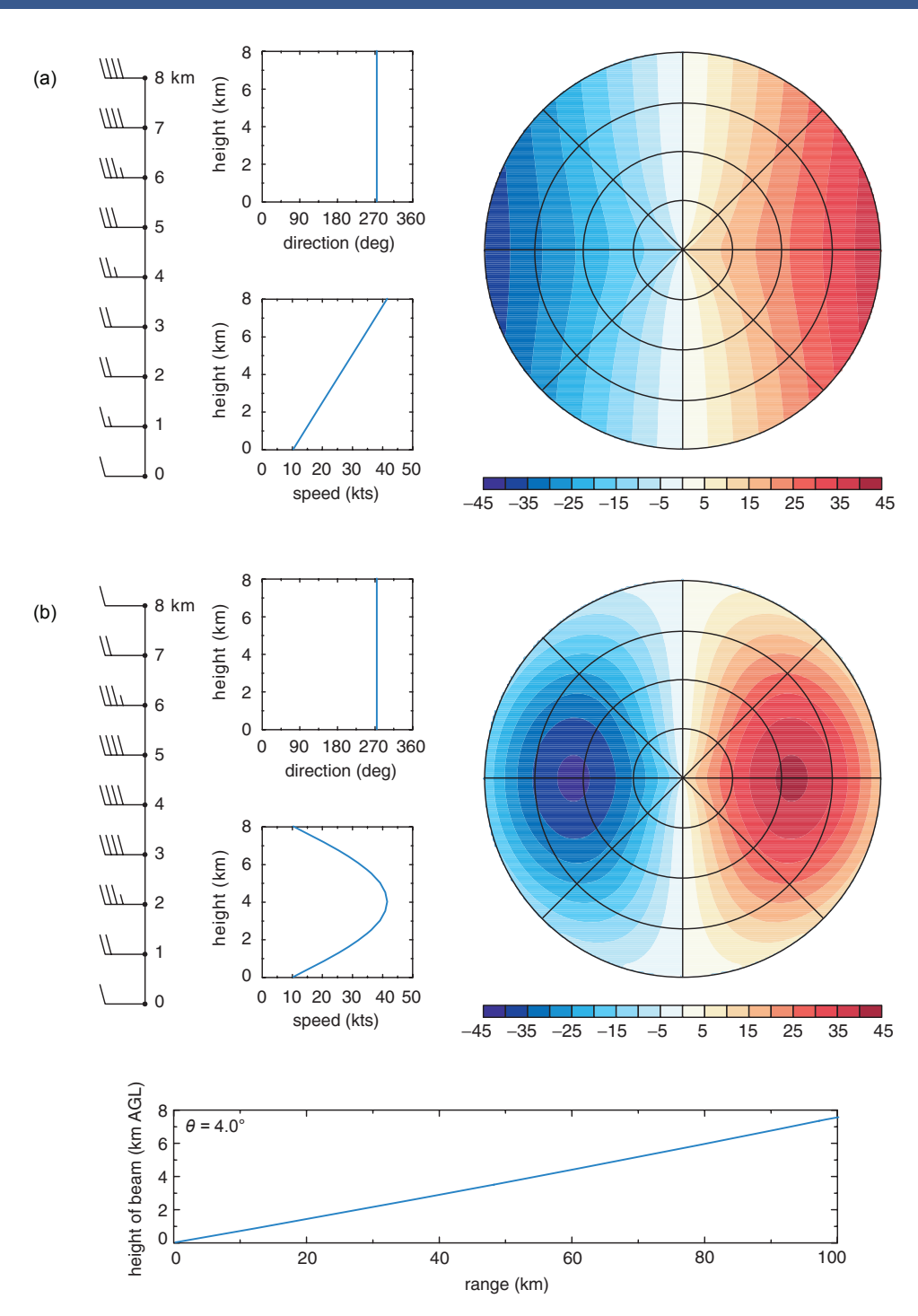
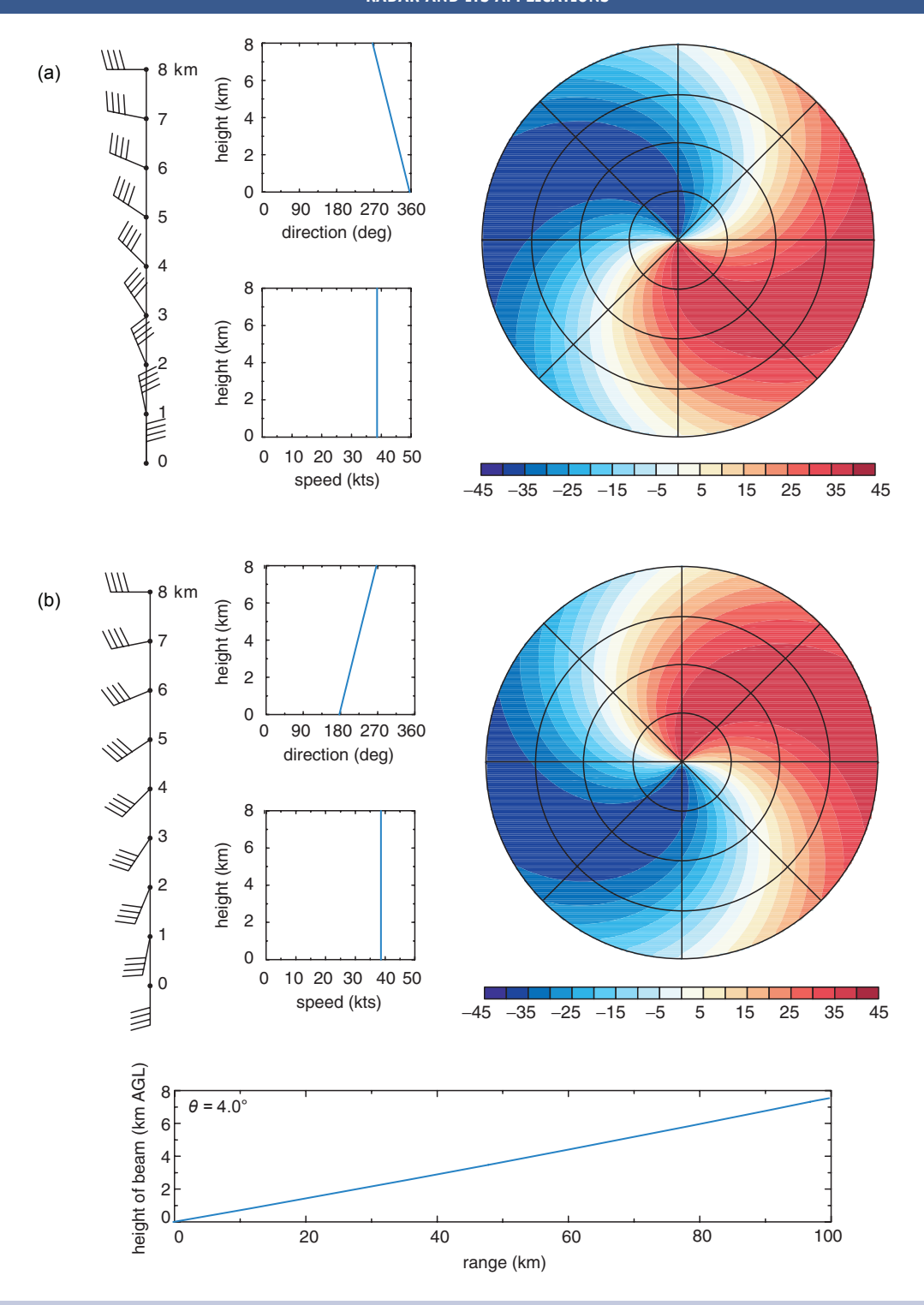


Figure A.10 (a) A velocity display in the presence of linear, unidirectional, westerly wind shear given an elevation angle of 4°. Range rings are drawn every 25 km and azimuth spokes are drawn every 45°. (b) As in (a), but for the case of unidirectional wind shear with a sinusoidal wind speed profile. The beam height versus range is displayed beneath (a) and (b).



10.10029780470682104.appt, Downloaded from https://onlinehtarry.wiley.com/doi/10.10029780470862104.appt by University Of newada Reno, Wiley Online Library of 1901/2024]. See the Terms and Conditions (https://onlinehtbarry.wiley.com/terms-and-conditions) on Wiley Online Library for rules of use; OA articles are governed by the applicable Ceative Commons License and Conditions (https://onlinehtbarry.wiley.com/terms-and-conditions) on Wiley Online Library for rules of use; OA articles are governed by the applicable Ceative Commons License and Conditions (https://onlinehtbarry.wiley.com/terms-and-conditions) on Wiley Online Library for rules of use; OA articles are governed by the applicable Ceative Commons License and Conditions (https://onlinehtbarry.wiley.com/terms-and-conditions) on Wiley Online Library for rules of use; OA articles are governed by the applicable Ceative Commons License and Conditions (https://onlinehtbarry.wiley.com/terms-and-conditions) on Wiley Online Library for rules of use; OA articles are governed by the applicable Ceative Commons License and Conditions (https://onlinehtbarry.wiley.com/terms-and-conditions) on Wiley Online Library for rules of use; OA articles are governed by the applicable Ceative Commons License and Conditions (https://onlinehtbarry.wiley.com/terms-and-conditions) on Wiley Online Library for rules of use; OA articles are governed to the applicable Ceative Commons (https://onlinehtbarry.wiley.com/terms-and-conditions) on the applicable Ceative Co

Figure A.11 (a) A velocity display in the presence of backing winds with height. As in Figure A.10, the elevation angle of the radar beam is 4°. Range rings are drawn every 25 km and azimuth spokes are drawn every 45°. (b) As in (a), but for the case of veering winds with height.

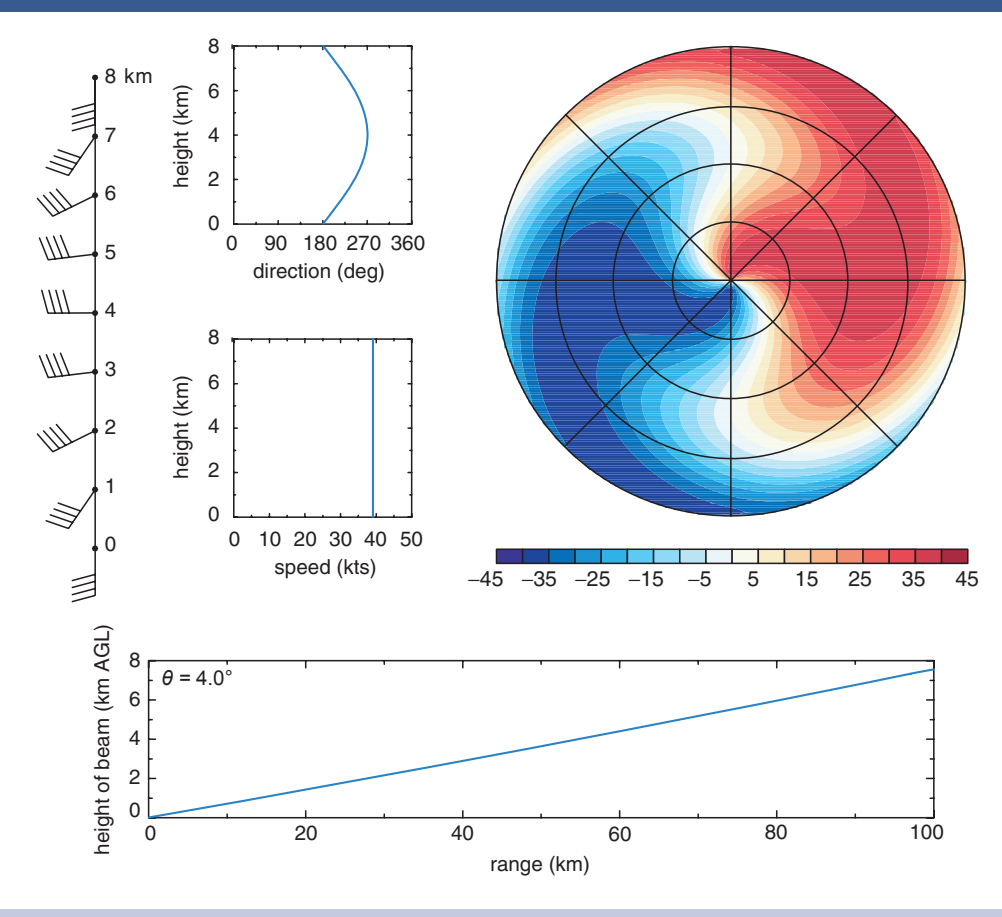


Figure A.12 As in Figure A.11, but for the case of veering winds with height overlain by a layer of backing winds with height.

convergence (Figure A.15c). Convergence/divergence and vorticity centers result in inbound-outbound radial velocity couplets, and the orientation of the couplets (i.e., the orientation of the zero radial velocity contour, or isodop, that separates the inbound and outbound velocities) relative to the radials is a function of the relative magnitudes of convergence and vorticity. Regions of high vorticity result in an inbound-outbound couplet that has its zero isodop oriented parallel to the radial that passes through the center of the couplet (Figure A.15a). Regions of purely convergent or divergent flow result in an inbound-outbound couplet that has its zero isodop normal to the radial that passes through the center of the couplet (Figure A.15b). A flow field that is both vortical and divergent/convergent has an inbound-outbound couplet with a zero isodop oriented at some intermediate angle with respect to the radial that passes through the center of the couplet (Figure A.15c).

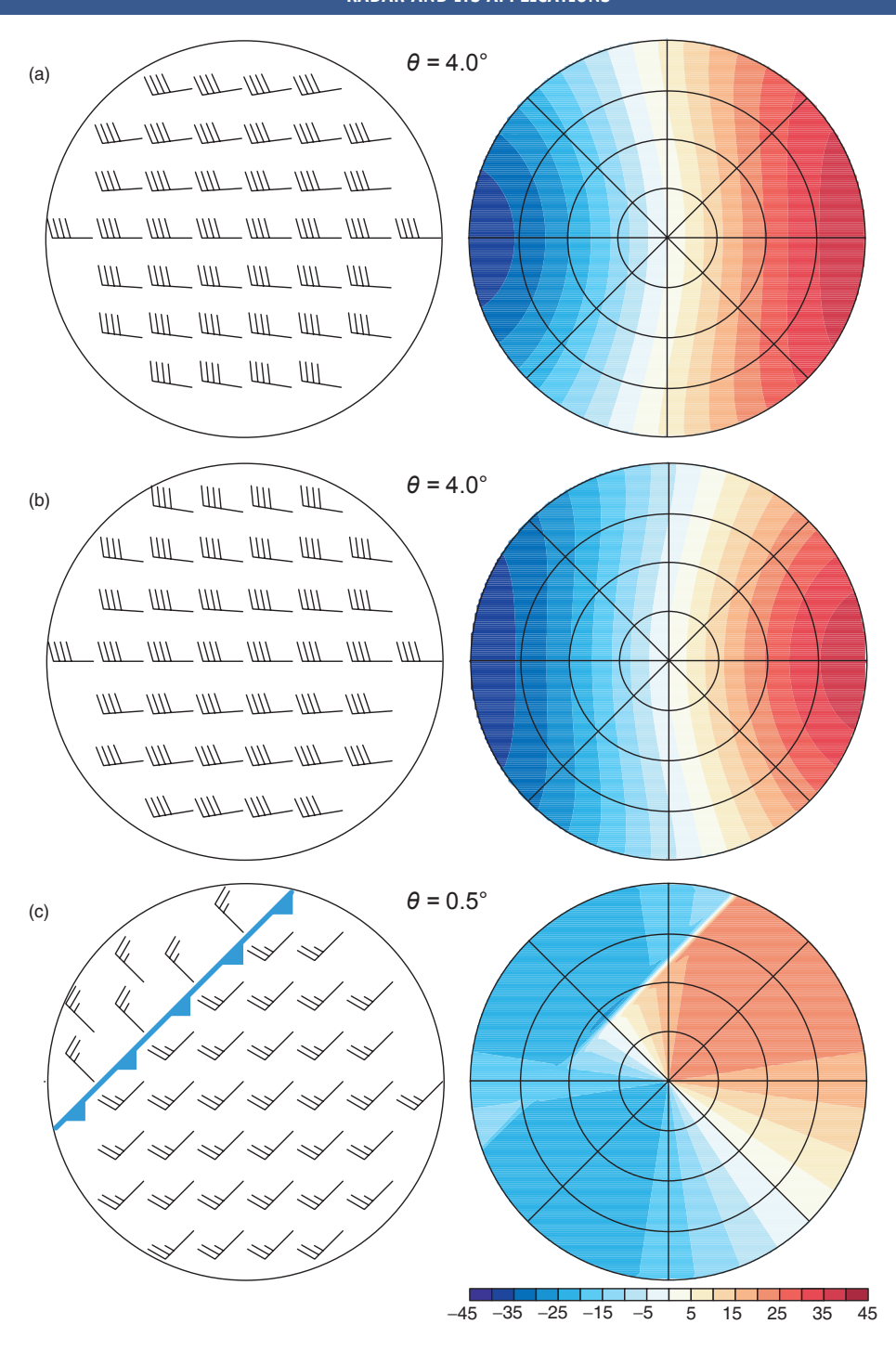
A.3.3 Estimating rainfall

Z-R relationships

The so-called Z-R method, which relates the logarithmic reflectivity factor Z to the rainfall rate R, is the simplest and most common way to estimate rainfall, because only measurements of reflectivity are needed. This technique assumes

$$Z = A R^B, (A.9)$$

where A and B are constants. The method is simple but prone to large errors, because the parameters A and B depend on the drop size distribution, which is generally not known with great accuracy. As an example, in stratiform precipitation, assuming a Marshall-Palmer drop size distribution leads to $Z = 200R^{1.6}$.



10.10027298470682104app, Downloaded from https://onlinelbitary.wike.com/doi/10.1002798470682104app1 by University Of Newada Reno, Wiley Online Library of 1901/2024, See the Terms and Conditions (https://onlinelbitary.wikey.com/erms-and-conditions) on Wiley Online Library or rules of use; OA articles are governed by the applicable Clearive Commons License

Figure A.13 Idealized Doppler velocity displays in the presence of horizontal inhomogeneity in the wind field. (a) A difluent wind field (left; horizontal cross-section is at 8 km) and its corresponding radial velocity display (right) for a 4° elevation angle. The wind speed increases linearly with height as in Figure A.10a. (b) The same as (a), but for a confluent wind field. (c) The case of a cold front approaching the radar from the northwest. Wind barbs in the horizontal cross-section (left) are at 0.5 km, and the corresponding radial velocity display (right) is based on a 0.5° elevation angle.

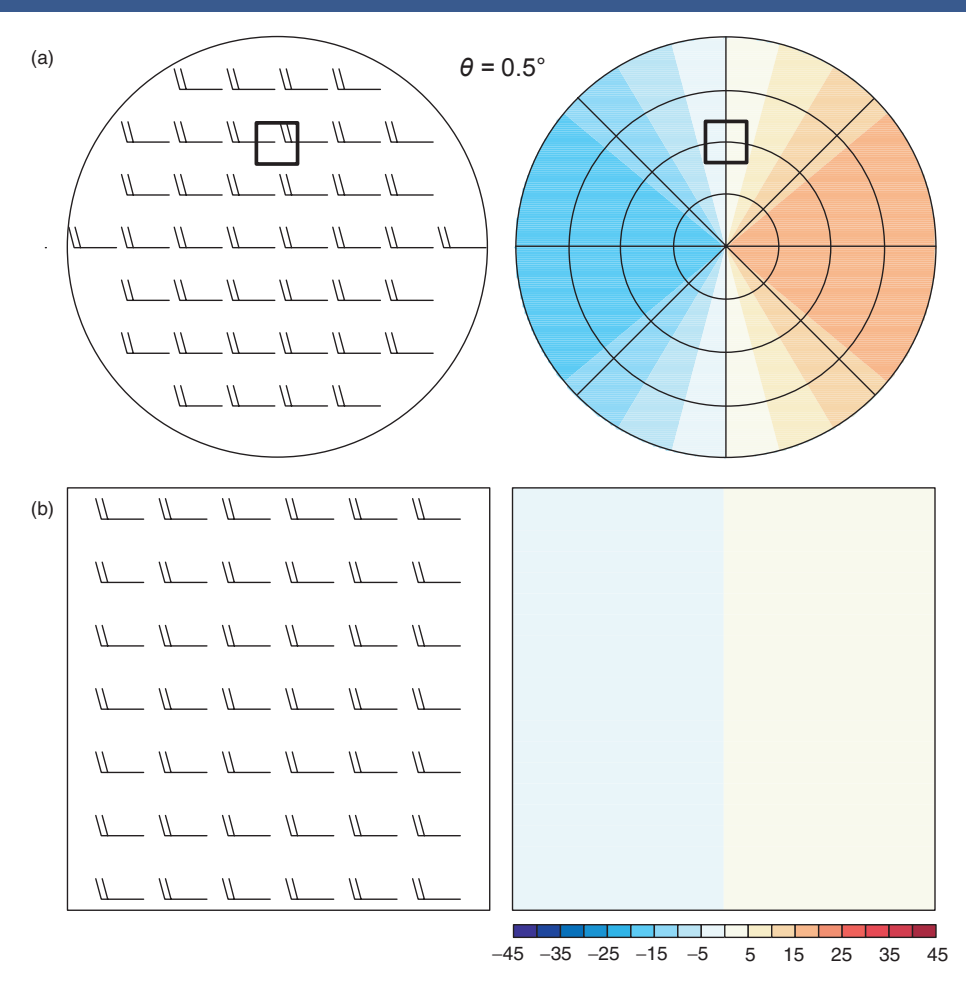


Figure A.14 (a) Idealized Doppler velocity display in the presence of uniform westerly low-level winds. On the left is a horizontal cross-section at $0.5 \, \text{km}$, and on the right is its corresponding radial velocity display (0.5° elevation angle). (b) The region enclosed by the box in (a) is cropped and enlarged. The enlarged region is $18 \times 18 \, \text{km}$ and is centered 50 km north of the radar.

One fundamental challenge in using *Z-R* relationships to estimate rain accumulations is that *Z* is proportional to the sixth power of the drop diameter, whereas *R* is proportional to the cube of the drop diameter (i.e., drop volume), such that there is no simple formula to relate the two quantities without knowing the size distribution of the hydrometeors. In addition to the uncertainty in knowing *A* and *B*, errors can also arise owing to the inability of the radar to make measurements near the ground beyond the radar horizon, calibration errors, incomplete beam filling, rainfall rate gradients, the presence of hail (large hail can invalidate the Rayleigh scattering approximation) or *bright bands* (Figure A.16), evaporation below cloud base, and the presence of strong updrafts (which suspend rainfall aloft).

When ice is present (either hail or bright bands), differences in the dielectric constant of liquid water compared with ice (liquid water is about nine times more reflective than ice at microwave wavelengths) can also contribute to the errors in precipitation estimation.

Dual-polarization radar

The polarization of an electromagnetic wave is defined by the orientation of the electric field wave crests. Conventional weather radars transmit and receive energy with a single, horizontal polarization; that is, the electric field wave crests are horizontal. *Dual-polarization* radars, on the other hand, transmit and receive both horizontally and

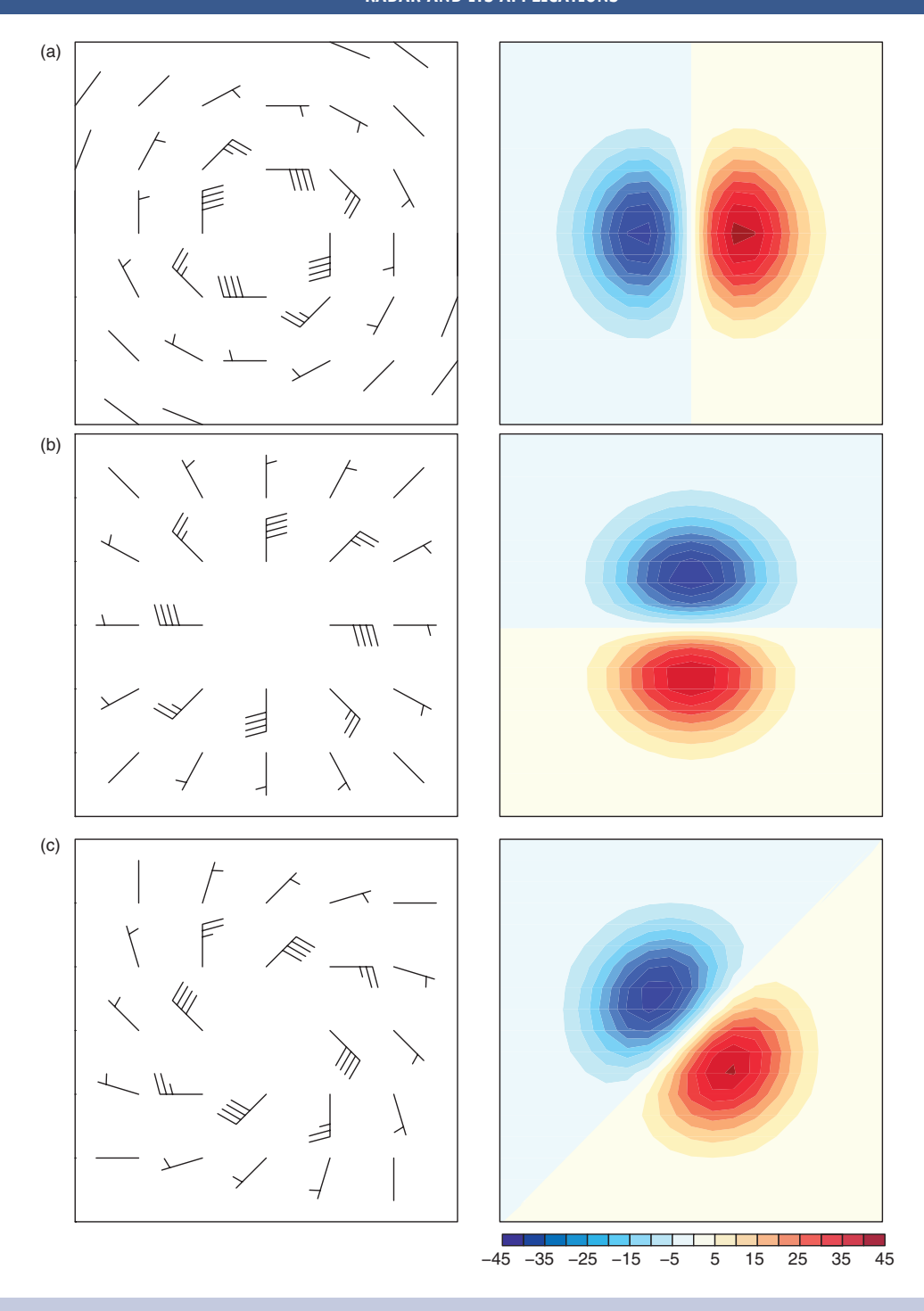


Figure A.15 (a) Idealized Doppler velocity display for the case of a mesocyclone having cyclonic vorticity (the radar is located to the south, e.g., the domain might be in the same location relative to the radar as the domain shown in Figure A.14). The elevation angle of the radar beam is 0.5° . Wind barbs are shown on the left and the Doppler velocity display is shown on the right. (b) As in (a), but for a purely convergent wind field. (c) As in (a), but for a wind field consisting of equal amounts of cyclonic vorticity and convergence.

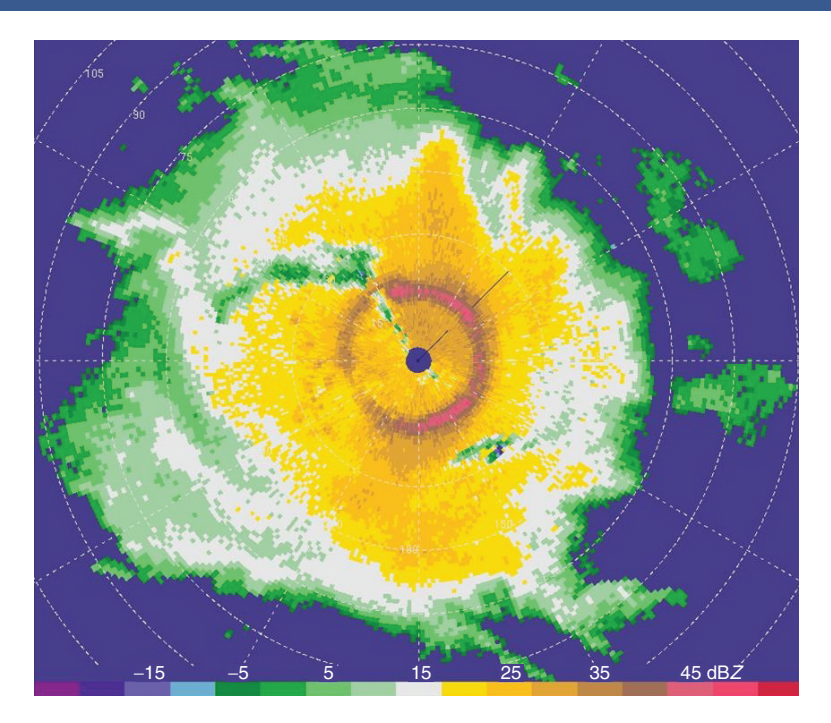


Figure A.16 As ice crystals form aloft and fall toward the surface, they collect each other to form large snowflakes. When the snowflakes start to melt upon reaching the melting level, they initially develop a water coating. Liquid water is about nine times more reflective than ice at microwave wavelengths, so these large wet snowflakes produce high reflectivity. Snowflakes with wet edges also readily clump together, forming large and highly reflective aggregates. As the flakes continue to fall and melt, they collapse into rain drops. The rain drops are smaller and fall faster, so both the size of the particles and their concentration are reduced, reducing the radar reflectivity. All of these processes lead to the formation of a narrow annulus of high reflectivity—a bright band—near the melting level that surrounds a radar scanning 360°.

vertically polarized pulses. Such radars can allow inferences to be made about the microphysical characteristics of precipitation regions (e.g., the drop size distribution) by way of differences between the horizontally and vertically polarized backscattered pulses. For example, reflectivity differences, or *differential reflectivity* ($Z_{\rm DR}$; measured in dB), can be used to estimate hydrometeor shape and therefore drop size, where

$$Z_{\rm DR} = 10 \log_{10} \left(\frac{z_{\rm hh}}{z_{\rm vv}} \right) = Z_{\rm hh} - Z_{\rm vv}.$$
 (A.10)

The h (v) subscripts indicate reflectivity factors associated with the horizontally (vertically) polarized pulses, and the first (second) subscript refers to the polarization of the transmitted (received) pulse. Hail and drizzle are nearly spherical and therefore backscatter the horizontally and vertically polarized transmitted pulses roughly equally, resulting in $Z_{\rm DR}$ values ~ 0 dB. Rain is associated

with $Z_{\rm DR}$ values \sim 2 dB. Snow is associated with $Z_{\rm DR}$ values \sim 1 dB. Melting bands are associated with $Z_{\rm DR}$ values \geq 3.5 dB. Conical graupel particles that are oriented vertically as they fall may be associated with negative $Z_{\rm DR}$ values. Information about the hydrometeor species can yield much better rainfall estimates than are possible with Z-R algorithms.

Other variables measured by dual-polarimetric radars are listed below.

Linear depolarization ratio The linear depolarization ratio (LDR) is the ratio of the power received in the channel that is orthogonal to the transmission channel, to the power received in the transmission channel. For example,

LDR = 10
$$\log_{10} \left(\frac{z_{hv}}{z_{hh}} \right) = Z_{hv} - Z_{hh}.$$
 (A.11)

LDR depends on the shape of the scatterer, among other things. LDR values typically range from approximately

−15 to −40 dB for meteorological targets (LDR approaches negative infinity for perfect spheres, but in real radars LDR values for small spheres are typically limited to roughly −40 dB owing to antenna limitations). LDR values can distinguish between rain, small hail, large hail, or a mixture of hydrometeor types. Large LDR, for example, suggests heavy rain mixed with hail.

Specific differential phase The specific differential phase $(K_{\rm DP})$ is the difference in the phase shift of the horizontally and vertically polarized waves owing to changes in the speed of the pulses as they travel through hydrometeors. Large $K_{\rm DP}$ values $(>4^{\circ}~{\rm km}^{-1})$ may indicate the presence of rain mixed with hail.

Co-polar correlation coefficient The co-polar coefficient (ρ_{hv}) is the pulse-by-pulse correlation between the

returned power of the horizontally and vertically polarized transmissions. In hail, $\rho_{\rm hv}$ is typically 0.90–0.95, although it can be >0.95 (<0.90) in small, dry hail (large, especially wet hail). In rain, $\rho_{\rm hv}$ is usually very large, often as large as 0.99; the exception is very light rain or drizzle, where a low signal-to-noise ratio can result in $\rho_{\rm hv}$ as low as 0.90. In mixed precipitation (including bright bands), $\rho_{\rm hv}$ is typically 0.90–0.95.

Dual-polarimetric variables are used collectively to develop hydrometeor classification algorithms (HCAs; Figure A.17). Not only do hydrometeor retrievals improve rainfall or snowfall estimates, but dual-polarimetric radar data show promise in large-hail and tornado detection as well (debris lofted by tornadoes has a unique

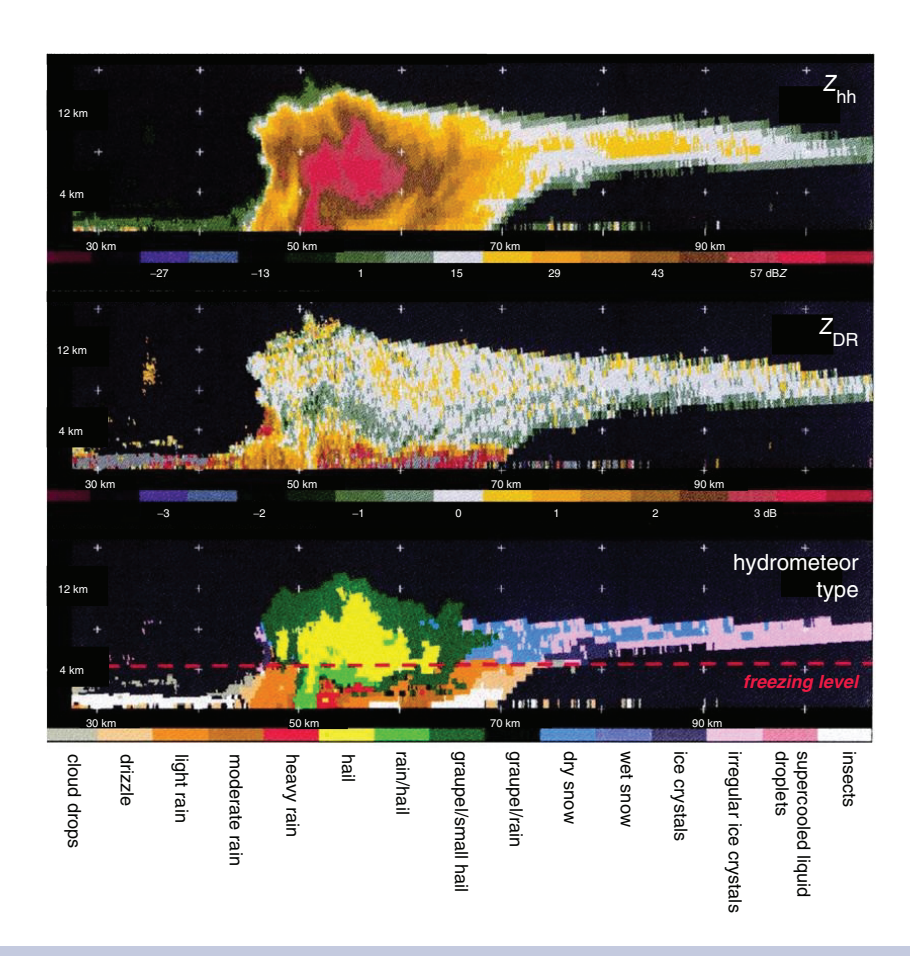


Figure A.17 Example of hydrometeor classification in a vertical cross-section of a thunderstorm using data from a dual-polarization radar (c); images (a) and (b) are reflectivity and differential reflectivity, respectively. Such classifications can improve rainfall estimations and perhaps warnings for severe hail and tornadoes as well. (From Vivekanandan *et al.* [1999]. Courtesy of the American Meteorological Society.)

APPLICATIONS 385

dual-polarimetric radar signature). It is anticipated that the WSR-88D network in the United States will be upgraded to a dual-polarization radar network in the next decade.

A.3.4 Dual-Doppler analysis

If two radars sample the same region quasi-simultaneously from different angles, the two-dimensional wind field can be retrieved (Figure A.18), and using a continuity equation, the full three-dimensional wind field can be retrieved. A wind synthesis obtained using two Doppler radars is referred to as a *dual-Doppler analysis* (Figure A.19).

The radar does not actually measure the wind motion at a point; rather, it measures the average speed of the hydrometeors toward or away from the radar in each sample volume. The fall speeds of hydrometeors therefore contribute to the measured radial velocity. Fall speeds are typically removed (somewhat crudely) by parameterizing the fall speeds in terms of the reflectivity. The resulting three-dimensional wind synthesis (and derivatives of the wind field, such as convergence and vorticity) can be adversely affected by the uncertainty associated with hydrometeor fall speeds.

The radial velocity v_R measured by one radar is

$$v_{\rm R} = u \cos \phi \sin \theta + v \cos \phi \sin \theta + W \sin \phi$$
, (A.12)

where ϕ is the elevation angle of the radar, θ is the azimuth angle of the radar, u and v are the horizontal wind components, and W is the sum of the actual vertical

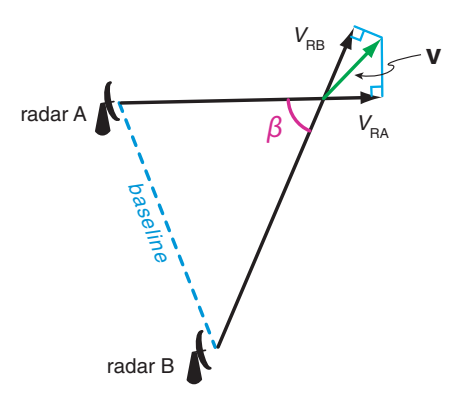


Figure A.18 Relationship between the radial wind components at radar A ($v_{\rm RA}$) and radar B ($v_{\rm RB}$), the baseline (dashed line), the between-beam angle (β), and the component of the wind velocity ${\bf v}$ in the plane defined by the radar radials.

velocity (w) plus some contribution from hydrometeor fall speeds (v_t) .

The above expression contains three unknowns: u_{i} v, and W. A three-dimensional wind synthesis is possible with two radars because two radars scanning the same location provide two independent radial velocity measurements at that location, and the use of the continuity equation, which couples the horizontal and vertical wind components, provides the third constraint on the three-dimensional wind (i.e., there are thus three knowns and three unknowns at each location scanned by two radars). Without becoming overly detailed, u, v, and w are obtained iteratively in regions scanned by two radars by computing the horizontal divergence, integrating the continuity equation, and parameterizing fall speeds in terms of Z. Solutions cannot be obtained along the line joining the two radars, referred to as the baseline, because the radial velocity measurements from the two radars are not independent at points along the baseline (i.e., the viewing angles of the radars are parallel along the baseline). Wind synthesis errors are typically unacceptably large wherever the between-beam angle (Figure A.18) is less than $20-30^{\circ}$ or greater than $150-160^{\circ}$; the three-dimensional wind retrieval is most accurate where the between-beam angle is 90°. Errors also are large when the elevation angle of either of the radars is too high (higher than $\sim 20-30^{\circ}$), or when the radial velocity data obtained by each radar are highly non-simultaneous (dual-Doppler data collection usually involves coordination between radars so that scanning is synchronized, i.e., both radars are scanning the same elevation at the same times at the target of interest.). With three or more radars, errors are reduced by fitting the synthesized wind field to the radial velocity observations in a least squares sense (this is sometimes called an over-determined dual-Doppler analysis).5

A.3.5 Thermodynamic retrieval

If three-dimensional, dual-Doppler wind syntheses are available at multiple times, temperature and pressure perturbations can be retrieved via a *thermodynamic retrieval*, sometimes simply called a *dynamic retrieval*. The horizontal

 $^{^5}$ With three or more radars, it is possible to obtain u, v, and W simultaneously, without iteration, and without the aid of the continuity equation. This approach is rarely used in practice, however, at least in the case of ground-based radars, because such radars scan at low elevation angles, which means that the radars sample the horizontal wind components much better than the vertical wind component. Such 'direct' multi-Doppler wind syntheses work best when each of the three velocity components is sampled well by at least one of the radars.

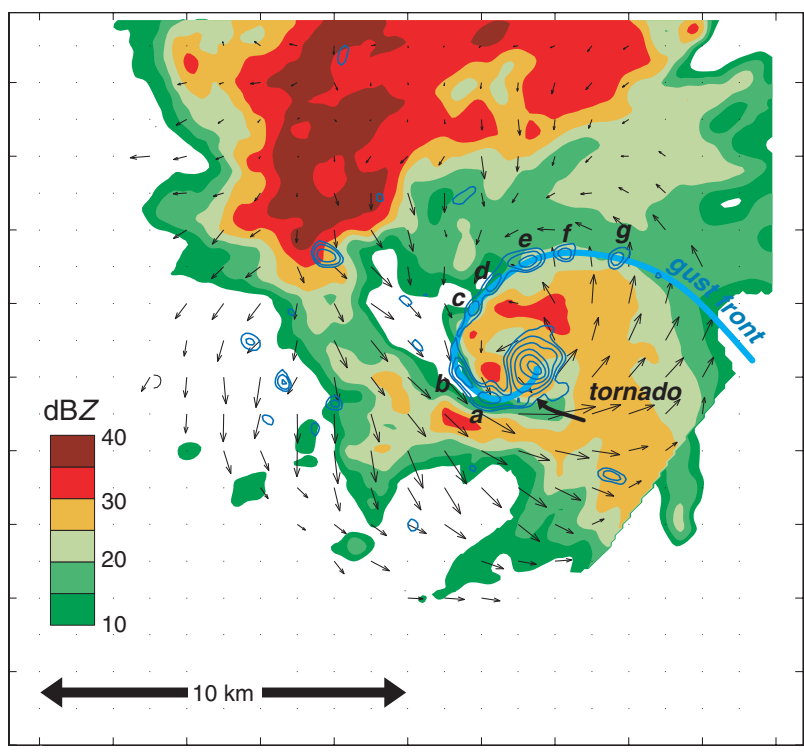


Figure A.19 Dual-Doppler wind synthesis based on Doppler On Wheels (DOW) observations of a tornadic supercell thunderstorm in south central Kansas at 0031 UTC 6 June 2001. Reflectivity (uncalibrated) is shown using the color shading. Isovorts at z=100 m are blue, and the rear-flank gust front is indicated with a bold blue line. Horizontal wind vectors at z=100 m are black. Vortices are evident along the rear-flank gust front (labeled a-g). The vortices were likely a result of horizontal shear instability, although vorticity stretching also likely contributed to the vorticity tendency significantly. Courtesy of Jim Marquis.

momentum equations can be written as

$$-\frac{\partial p'}{\partial x} = \overline{\rho} \left(\frac{\mathrm{d}u}{\mathrm{d}t} - fv - F_u \right) \tag{A.13}$$

and

$$-\frac{\partial p'}{\partial y} = \overline{\rho} \left(\frac{\mathrm{d}v}{\mathrm{d}t} + fu - F_v \right),\tag{A.14}$$

where u and v are the zonal and meridional wind components, p' is the pressure perturbation, $\overline{\rho} = \overline{\rho}(z)$ is a reference density profile, f is the Coriolis parameter, F_u and F_v represent the effects of turbulent drag, and $d/dt = \partial/\partial t + \mathbf{v} \cdot \nabla$. At each vertical level, the Coriolis, momentum advection, and turbulent drag terms (via parameterization) can be obtained from the dual-Doppler wind synthesis. The local accelerations $\partial u/\partial t$ and $\partial v/\partial t$ can be estimated

from a series of three-dimensional wind syntheses. The reference density profile can be obtained from a nearby sounding.

10.10027280470862104.app, I. Downloaded from https://onlinelbrlary.wiley.com/doi/10.10027980470862104.app1 by University Of Newada Reno. Wiley Online Library on [1901/2024]. See the Terms and Conditions (https://onlinelbrlury.wiley.com/terms-and-conditions) on Wiley Online Library or rules of use. OA articles are governed by the applicable Certain Common Library on [1901/2024]. See the Terms and Conditions (https://onlinelbrlury.wiley.com/terms-and-conditions) on Wiley Online Library for rules of use. OA articles are governed by the applicable Certain Common Library on [1901/2024]. See the Terms and Conditions (https://onlinelbrlury.wiley.com/terms-and-conditions) on Wiley Online Library on [1901/2024]. See the Terms and Conditions (https://onlinelbrlury.wiley.com/terms-and-conditions) on Wiley Online Library wiley.

Because the rhs of (A.13) and (A.14) is known, the horizontal pressure gradients $\partial p'/\partial x$ and $\partial p'/\partial y$ are therefore also known; p' can be obtained at each level by taking $\partial(A.13)/\partial x + \partial(A.14)/\partial y$ and inverting $\nabla_h^2 p' = \partial^2 p'/\partial x^2 + \partial^2 p'/\partial y^2$, usually applying Neumann boundary conditions on the horizontal boundaries of the dual-Doppler domain. If Neumann boundary conditions are used, then the retrieved p' field is not unique. However, the horizontal gradients of p', which are unique, are typically of greater interest than p' itself.

It can be shown that the field of $p' - \langle p' \rangle$ is unique, where $\langle p' \rangle$ is the horizontal average of the retrieved p' at each level. If $p' - \langle p' \rangle$ is vertically differentiated, it can be

used to retrieve information about the buoyancy field via

$$B - \langle B \rangle = \left(\frac{\mathrm{d}w}{\mathrm{d}t} - F_w\right) - \left(\frac{\mathrm{d}w}{\mathrm{d}t} - F_w\right) + \frac{1}{\overline{\rho}} \frac{\partial}{\partial z} (p' - \langle p' \rangle),\tag{A.15}$$

where w is the vertical velocity, B is the buoyancy, F_w is turbulent drag, $\langle B \rangle$ is the average of the retrieved buoyancy at a given level, and $\langle \frac{\mathrm{d}w}{\mathrm{d}t} - F_w \rangle$ is the average $\frac{\mathrm{d}w}{\mathrm{d}t} - F_w$ at a given level. Equation (A.15) is obtained by subtracting the horizontally averaged vertical momentum equation from the unaveraged vertical momentum equation. At each vertical level, $\frac{\mathrm{d}w}{\mathrm{d}t} - F_w$ and $\langle \frac{\mathrm{d}w}{\mathrm{d}t} - F_w \rangle$ can be obtained from the dual-Doppler wind syntheses. Because all of the terms on the rhs are unique, $B - \langle B \rangle$ on the lhs is also unique. However, B is not unique, as was the case for the retrieved B field. Nonetheless, the *pattern* and *gradients* of the retrieved B field on a horizontal plane are unique (B and $B - \langle B \rangle$ differ only by a constant on a horizontal plane), which is often of significant value. Ambiguities regarding the uniqueness of the B field can be resolved if independent *in situ* observations are available at each level.

Thermodynamic retrievals commonly are performed in mesoscale observational studies when high-quality multiple-Doppler radar data are available. They can be valuable because in situ measurements of temperature and pressure often cannot be obtained easily, especially above the ground. However, there are limits to the quality of the retrieved pressure and buoyancy fields. The retrieved pressure and buoyancy fields are intrinsically less accurate than the synthesized wind fields because of all of the differentiations involved (the buoyancy retrieval involves one more differentiation than the pressure retrieval; therefore, the retrieved buoyancy field is usually less reliable the pressure field). Moreover, poor temporal resolution (e.g., several minutes may elapse between volume scans of a storm) leads to errors in the estimation of $\partial \mathbf{v}/\partial t$, and the parameterization of turbulent drag also introduces uncertainty. In the end, even decent-looking dual-Doppler-derived horizontal wind fields can result in poor buoyancy fields. Thus, direct measurements of temperature and pressure are virtually always important components of mesoscale observational studies.

Further reading

Bluestein, H. B., and R. M. Wakimoto, 2003: Mobile radar observations of severe convective storms. *Radar and Atmospheric Science: a Collection of Essays in Honor of David Atlas, Meteor. Monogr.*, No. 52, 105–138.

Burgess, D., and P. S. Ray, 1986: Principles of radar. *Mesoscale Meteorology and Forecasting*, P. S. Ray, Ed. Amer. Meteor. Soc., 85–117.

Chandrasekar, V., R. Meneghini, and I. Zawadzki, 2003: Global and local precipitation measurements by radar. Radar and Atmospheric Science: a Collection of Essays in Honor of David Atlas, Meteor. Monogr., No. 52, 215–236.

Doviak, R. J., D. Sirmans, and D. S. Zrnic, 1988: Weather radar. *Instruments and Techniques for Thunderstorm Observation and Analysis*, E. Kessler, Ed., 2nd edn. University of Oklahoma Press, 137–169.

Doviak, R. J., and D. S. Zrnic, 1993: *Doppler Radar and Weather Observations*. Academic Press, 562 pp.

Hane, C. E., C. L. Ziegler, and P. S. Ray, 1988: Use of velocity field from Doppler radars to retrieve other variables in thunderstorms. *Instruments and Techniques for Thunderstorm Observation and Analysis*, E. Kessler, Ed., 2nd edn. University of Oklahoma Press, 215–234.

Raghavan, S., 2004: *Radar Meteorology*. Springer, 537 pp. Rinehart, R. E., 20xx: *Radar for Meteorologists, Fourth Edition*. Rinehart, 428 pp.

Sauvageot, H., 1992: *Radar Meteorology*. Artech House, 384 pp.

Vivekanandan et al. (1999).